Electrohydrodynamic Jet Printed 3D Metallic Grid: Toward High-Performance Transparent Electrodes

Bin Zhang, Hyungdong Lee,* and Doyoung Byun*

2D metallic grids that consist of various nanomaterials that are suitable for the replacement of indium tin oxide in transparent electronics (TEs) manufacturing. High-resolution conductive grids with large open areas are often required while considering high transmittance. However, previous research shows that this kind of TE often cannot have high transmittance and low sheet resistance simultaneously; it hinders the fabrication techniques and materials from practical applications. Herein, direct fabrication of a high-performance TE through electrohydrodynamic jet 3D printing technique is reported. Micro-scale 3D metallic grids with an aspect ratio of above-5 were printed on a polyester film using Ag nanoparticles. The metal grids with high aspect ratios exhibit an average sheet resistance of $3 \, \Omega \, sq^{-1}$ and transparency of 96%. Both optical and electrical performances are significantly enhanced for which the large cross-section of the metallic grid is contributed. Furthermore, the flexibility of printed TE is also characterized by the bending and recovering test. It is believed that the printed flexible TE, which utilize a high aspect ratio, 3D metallic grids may replace the conventional ITO glass for which both high transmittance and conductivity are achieved with economic efficiency.

Transparent electrodes (TEs) are critical in the operation of various transparent optoelectronic devices, including solar cells, electroluminescent and electrochromic devices, and touch screen panels.[1–3] Nowadays, metal oxides are the most common materials that are used for the fabrication of TEs.[4] Indium tin oxide (ITO), particularly, is highlighted as the most widely used transparent conductive material due to its considerable conductivity and good optical transmittance, which nearly comprises 90% of the global market.[2,5] However, indium is abundant in the earth's crust (0.05 ppm), and its cost has risen in order of magnitude over the past decade.[6] Moreover, some disadvantages such as high cost and inherent brittleness of ITO renders it unsuitable for the next-generation highly conductive and flexible optoelectronic applications.[7,8]

The alternatives to ITO have been actively developed, such as conducting polymers, graphene, carbon nanotubes, metal nanowire (NW), and nanoparticle (NP) networks.[9–17] Although the polymeric material shows great prospects in flexible TE fabrication, its electrical conductivity and visible light transmittance are too low to meet the requirements of a high-performance TE in future applications.[18] In particular, metallic TEs, including NW networks and micro/nanoscale 2D metallic NP grids, provide superior electrical and optical properties in comparison to other materials.[19–24] These metallic material-based transparent conducting electrodes demonstrate excellent performances with respect to electrical resistance and mechanical bending due to their intrinsic metallic properties. There are several reports on possible alternatives to obtain high-performance TEs by taking advantages of Ag-NWs and incorporating Ag-NPs networks.[25,26] The sheet resistance (R_s) and optical transmittance (T) performance have been systematically investigated. When compared with randomly distributed metal NWs, the metal grid is more uniform and does not suffer from wire-to-wire junction resistance.[27] However, the transparent electronics (TEs), which consisted of metallic grids require large open area to guarantee the optimal T. The critical issue of such 2D metallic grid is that the charges generated from the large area of empty spaces within the grid cannot be efficiently collected. As a result, the R_s would increase due to this trade-off relation.[28,29] Therefore, common transparent electrodes cannot have high transmittance and low sheet resistance simultaneously.

To date, several reports have demonstrated that compared with the traditional 2D pattern, a 3D metallic grid may provide us an alternative solution so that both the optical and electrical performances could be enhanced due to the large cross-section of the 3D structure.[30] However, the fabrication process of high-resolution 3D conductive structures on various transparent substrates consists of the multi-step sequence, such as photolithographic and chemical processes that are environmentally hazardous, toxic, and uneconomical.[31,32] Hence, direct 3D printing techniques have emerged creditably due to their cost-effectiveness and simplicity, given the number of step sequences, compared with the conventional fabrication process.[33,34] Among these, the electrohydrodynamic (EHD) jet printing technology has been highlighted as an effective technique for the construction of high-resolution conductive structures for electronic devices.[35,36] Often, a rheological behavior ink suspension containing metallic NPs, such as Ag-NP and Au-NP, can be operated at room temperature. Driven by a strong electrostatic

Dr. B. Zhang, Dr. H. Lee, Prof. D. Byun
Dept. of Mechanical Engineering
Sungkyunkwan University
2066 Seobu-Ro, Jangan-Gu, Suwon 440–746, Republic of Korea
E-mail: cloud101@skku.edu; dybyun@skku.edu

The ORCID identification number(s) for the author(s) of this article can be found under https://doi.org/10.1002/adem.201901275.

ADVANCED
SCIENCE NEWS
www.advancedsciencenews.com

ADVANCED
ENGINEERING
MATERIALS
www.aem-journal.com

force, the ink could overcome the capillary pressure and surface tension continuously deposited on various substrates with the noncontact method. The resolution of the printed patterns could be significantly improved by using a ultra-fine Taylor-cone jet.[29]

Herein, we report a novel strategy for direct fabrication of highly transparent and conductive electrodes via the EHD jet 3D printing technique. The Ag-NPs were repeatedly printed on polyester films. Few micro-scales 3D metallic grids with aspect ratios above-5 were fabricated layer-by-layer. The highly conductive metal grids exhibited an average sheet resistance of about 3 Ω sq^{-1} and transparency of 96%. Both the sheet resistance and transmittance of the transparent electrode were significantly improved for which the large cross-section of the 3D pattern was contributed. Moreover, the flexibility of the printed TE was also characterized by the bending and recovering test. It is believed that the proposed TE based on EHD jet-printed 3D metallic grids may replace the conventional ITO glass, for which both high transmittance and conductivity are achieved with economic efficiency.

A high viscosity Ag-NP and polyethylene oxide (PEO) composite that is based on a commercialized Nano-paste (EM-SP01, EnJet Inc.) was served as the ink. The Ag-NPs concentration was 70% by weight. The PEO (400 000 MW) was diluted by chloroform (Sigma Aldrich, USA) by a solid content of 15 wt%. Then, we mixed the Ag-NPs Nano-paste with PEO solution by a ratio of 4:1 so as to reduce the electrical conductivity and avoid system breakdown during printing. The ink was precisely infused into a stainless-steel nozzle using a syringe pump of the EHD jet printer (X-model, www.enjet.co.kr) (**Figure 1**a). To generate a continuous ejection of the high-viscous ink containing Ag-NPs and polymer composite, a high-voltage amplifier was included in the printing system. A direct current (DC) voltage was applied onto the nozzle to form a strong electric field that drives the ink to form an ultra-fine filament toward the substrate. The schematic that illustrates the process of 3D metallic grid fabrication is shown in Figure 1b. The distance between the stainless-steel nozzle and target substrate was adjusted using a Z micro-stage. The XY micro-stage allows for an accurate positioning and reciprocating motion of the target substrate. The magnified inset shows a fine jet stream form at the nozzle tip and layer-by-layer deposited on the substrate and forms the 3D grid over a large area. As the solvent evaporates after extrusion, the rigidity of the filament gradually increases with time due to a locally higher polymer concentration.[37] This rigidity gradient enables the creation of self-supporting 3D structures by changing the printing parameters, such as the nozzle–substrate distance and printing speed (printing parameters). After evaporation of majority of the solvent, the rigidity of the extruded filament changes from fluid-like to solid-like, which facilitates the shape retention of the deposited self-supporting 3D structures. This 3D printing technique enables the fabrication of large areas of 3D metal grid geometries with high efficiency.

The 3D printing presented in this study was developed to fabricate 3D metallic grids at room temperature with dissolvable polymers. For successful 3D printing that is based on the solvent-cast process, the selected solvent and polymer concentration in the solution have to be set to ensure proper ink rheological behavior while providing a fast solvent evaporation. Then, the applied electrostatic force on the ink must be tailored to achieve a linear flow rate. During the construction of the 3D structures, the solvent evaporation condition of the jetting filament greatly influenced the printing resolution, aspect ratio, conductivity, and mechanical strength of the 3D structures. First, the solvent molecules must move through the filament and then evaporate at the air/filament interface. If the solvent evaporation process is not appropriate, a deformation and collapse of a 3D structure could occur, which is due to the slow evaporation rate of the solvent.[38] To guarantee that the solvent will evaporate into the surrounding air during the printing, the Biot number (Bi), which gives an index of the ratio of the internal diffusion resistance to the external convection resistance, was calculated during the filament jetting, as

$$Bi = hd\alpha/D_{ss} \tag{1}$$

where, h is the convective mass-transfer coefficient [mm/s], d is the filament diameter [mm], α is the partition coefficient between the two phases at the interface, and D_{ss} is the internal solvent-diffusion coefficient [mm^2/s]. The value of α is estimated as the ratio of the partial density of the solvent on the vapor side to that on the liquid side (or the vapor–liquid equilibrium) ($\alpha \approx 10^{-3}$), as reported by Kojic et al. (2004).[39,40] Since the solvent concentration exerts a great influence on D_{ss}, a representative order of the magnitude of $D_{ss} \approx 10^{-5}$ mm^2 s^{-1} was taken. It is known that h depends on the velocity and geometry of the ink solution. For a continuous jet, the Sherwood number (the ratio of the convective mass transport to the diffusive mass transport) $Sh = hd/D_{sair} \approx 0.3$ produced the value $hd \approx 0.3 D_{sair}$, where d is the filament diameter ($d \approx 3$ μm according to the photo captured by a CCD camera), and D_{sair} is the solvent–vapor diffusion coefficient through the air and is normally taken as $D_{sair} \approx 10$ mm^2 s^{-1}; therefore, $hd \approx 3$ mm^2 s^{-1}. Finally, the calculated mass-transfer Biot number is for the droplet, $Bi \approx 300 >> 1$, indicating that the internal diffusive resistance dominates the evaporation process, and the convection is negligible in this case. This indicates that the solvent in the filament could be dried out upon its arrival on the substrate for the formation of the 3D grid, as observed in the experiments.

The grids are fabricated layer-by-layer through consecutive overprints, giving complete control over the aspect ratio and localized pattern. The effects of the various printing conditions, such as high voltage, working distance and printing speed on the pattern resolution, were fully investigated to find the optimal printing condition. The primary-parameter number of layers effect on the grid height and width are shown in Figure 1c,d, respectively. A DC voltage of 2.5 kV was applied on a stainless-steel nozzle with a 150 μm inner diameter. The working distance between the nozzle and substrate was fixed at 1000 μm to provide enough space for the ink solvent evaporation. The 3D micron-scale grids with different aspect ratio were achieved with multilayers ranging from 1 to 25. The inset photo, which was captured by a microscope, shows the increase in pattern width, whereas the number of printed layers increased from 1 to 20 (Figure 1c). We could also notice that the width increased significantly when the number of layers was less than 5. This is mainly due to the surface tension during the ink contact with the polyester film. The width increased and height hardly changed, correspondingly. However, the width of the 3D metallic grid
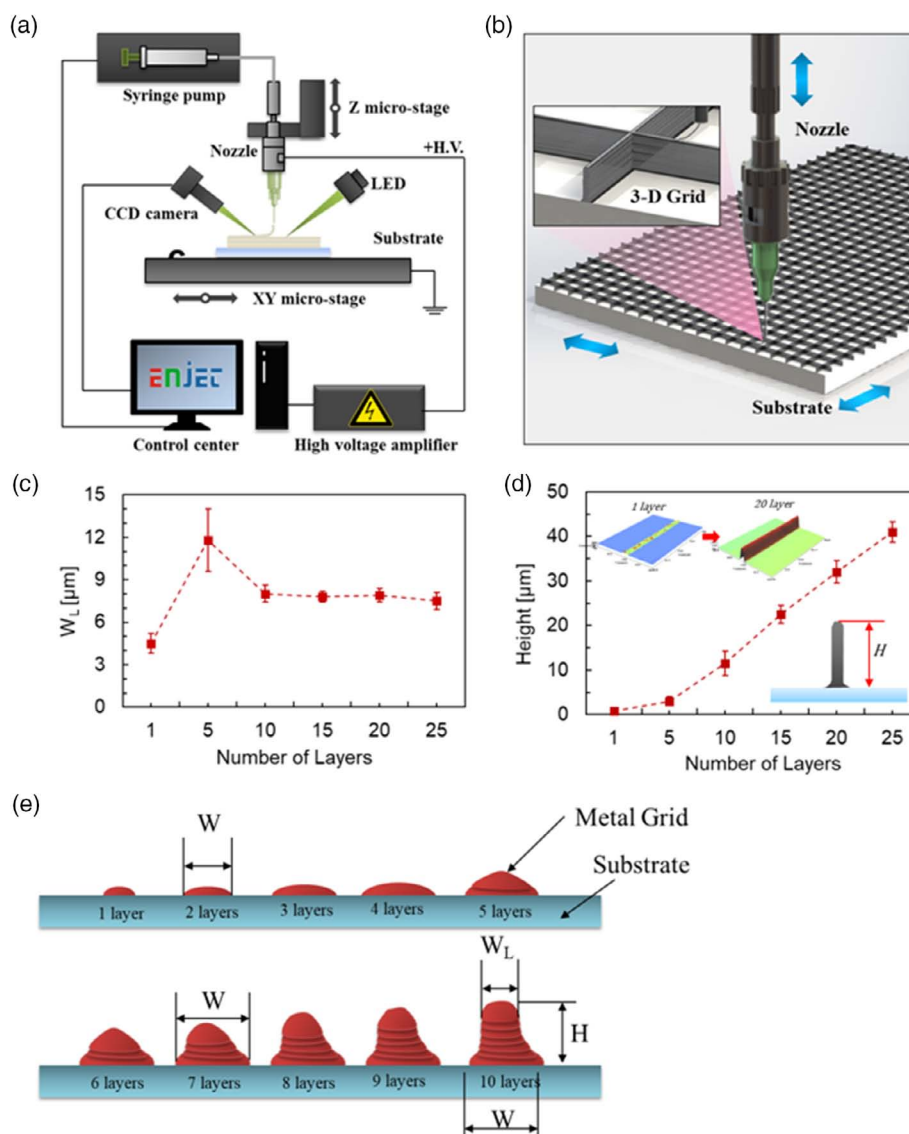
Figure 1. Schematic diagrams summarizing the fabrication process of a 3D metallic grid using the EHD jet-printing technique. a) The Schematic illustrates the 3D printing system (X-model, www.enjet.co.kr). b) The magnification of the 3D-printed high aspect-ratio metal grid on the substrate. c) The grid width by different number of printed layers (W_L). The inset photo that was captured by a microscope shows the pattern width increase, whereas the number of printed layers increased from 1 to 20. d) The relationship between the number of printed layers and metal grid height. The inset shows the comparison of height, whereas the number of printed layers increase from 1 to 20. e) Illustration of the parameters of the metal grid (cross-section): Pattern width (W); width by different layers (W_L); height (H).

remained constant along those heights regardless of the height, where the number of printed layers was from 10 to 25. This indicated that the ink solution became solid before its arrival on the target substrate. If the ink solvent does not fully evaporate before its arrival on the target substrate, it should spread over the substrate because of the surface tension. Therefore, the solvent evaporates into the surrounding air during jetting. Furthermore, this phenomenon is also due to the different electrical conductivity of the substrate. Compared with the original polyester film, the printed Ag-NPs act as the metallic substrate after the solvent evaporation. We have proved that Joule heating occurs at the interface between the Ag-NPs during EHD jet printing.[38,41] The temperature that arises around the contact

area results in the acceleration of the solvent evaporation speed. This result can also be proved by the effect of the number of layers on the height, as shown in Figure 1d. The height increased with the number of layers, reached peak value at the layers ranging from 5 to 10. The relationship between the height and number of layers was approximately linear afterward. However, the height increase is less noticeable in the early stage. The inset 3D profile images indicate the height difference, whereas the number of printed layers increased from 1 to 20. The cross-section area increased significantly. An illustration of the parameters of the metal grid (cross-section) and the 3D structure formation process is shown in Figure 1e.

The fundamental idea behind using high aspect-ratio 3D metal grids as high-performance TEs is to increase the pattern cross-section without increasing the shadowing area. Figure 2a shows the actual photograph of the highly transparent polyester films, which consist of 3D grids with different aspect ratios. The number of printed layers were 0, 1, 10, and 20, respectively. A sheet of paper with printed SKKU logos was placed underneath the polyester films to illustrate the transparency through which the logo on the paper underneath can be clearly seen. The transparency of the TE slightly decreased while increasing the number of layers. To further investigate the surface morphology of the 3D-printed metal grid, we used a microscopic photo and scanning electron microscopy (SEM) topography images to show the structures in detail. Figure 2b shows an optical image of the Ag grid on the PET film substrate with a spacing of 500 μm. In this study, we fabricated square grids on the PET film, and the geometrical parameters of its shadowing area are described in Figure 2c. P is the grid pitch and W is the width of the grid. These dimensions could also further contribute to the estimation of the transmittance. The morphology and microstructure of the 3D metal grid-based TE is further characterized by SEM, as shown in Figure 2d,e. The printed layer was over 25 and tilted captured SEM images show the square-shaped high aspect-ratio 3D grid over the large area. The average width of the grid is 8 μm. Due to the surface tension of the ink, the pattern width slightly increased at the beginning. However, it later remained constant during the continuous increase in height because of the self-sintering that occurred between the Ag-NPs (Figure 2e) as we previously demonstrated. The Ag-NPs densely aggregated and formed a uniform 3D grid. The width hardly changed along the height. Therefore, the TEs can have both high conductivity and transmittance without increasing the shadowing area.

Figure 3 shows the optical properties of the 3D metal grid on the PET film substrates. Figure 3a,b exhibit the total and diffused transmittance of the number of printed layers ranging from 1 to 25 in the wavelength range from 300 to 800 nm, respectively. All the Ag grids had 500 μm pitch and total transmittance of over 96%. The printed film had total transmittance values of 97.8% and 96.8% for 5 and 10 layers, averaged over the entire wavelength range. The 3D grid height is controlled by the number of printed layers. The more the repeat in the printing cycle, the higher the grid. In the beginning, the transmittance decreased significantly compared with the bare PET film. However, as the thickness increased over 10 layers, the transmittance hardly changed (Figure 3b). The transmittance decreased by about 0.8% with 15 layers of Ag pattern. This indicated that with the increase in the grid aspect-ratio, the transmittance of the printed TE does not markedly decline. Therefore, after 25 layers of printing, the T still remains over 96%. This phenomenon matched very well with the cross-section morphology of the 3D grid. The shadowing area of the grid is the key factor that affects the transmittance of the 3D-printed TEs. The aspect-ratio of the 3D grid increased, whereas the width remained constant. Therefore, a high transmittance could be achieved. For the square grid, the shadowing area can be expressed by the geometrical fill factor

$$F_f = \frac{P \times W + (P - W) \times W}{P^2} \tag{2}$$

where P is the pitch and W is the width of the grid, respectively (Figure 2c). From the fill factor, it is possible to predict the transparency by using
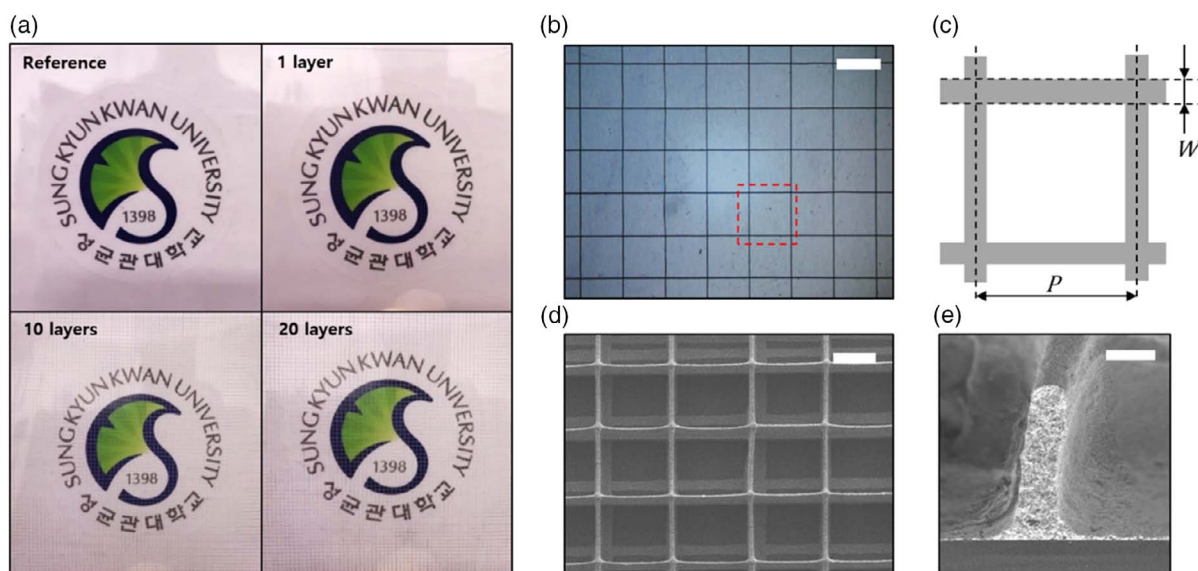

Figure 2. The morphology of the TE fabricated by EHD jet printing. a) The real photograph of a highly transparent polyester film that consists 3D grids. The number of printed layers was 0, 1, 10, and 20, respectively. A sheet of paper with SKKU logos placed underneath the films to demonstrate the transparency b) Optical micrograph showing the metallic grid produced by EHD jet printing over a large area. The scale bar is 500 μm. c) The illustration of the grid width and pitch. d) Tilted SEM image (30°) of the 3D metallic grid. The scale bar is 200 μm. e) Cross-section SEM image of the grid. The width of the structural hardly changes with its height. The scale bar is 10 μm.
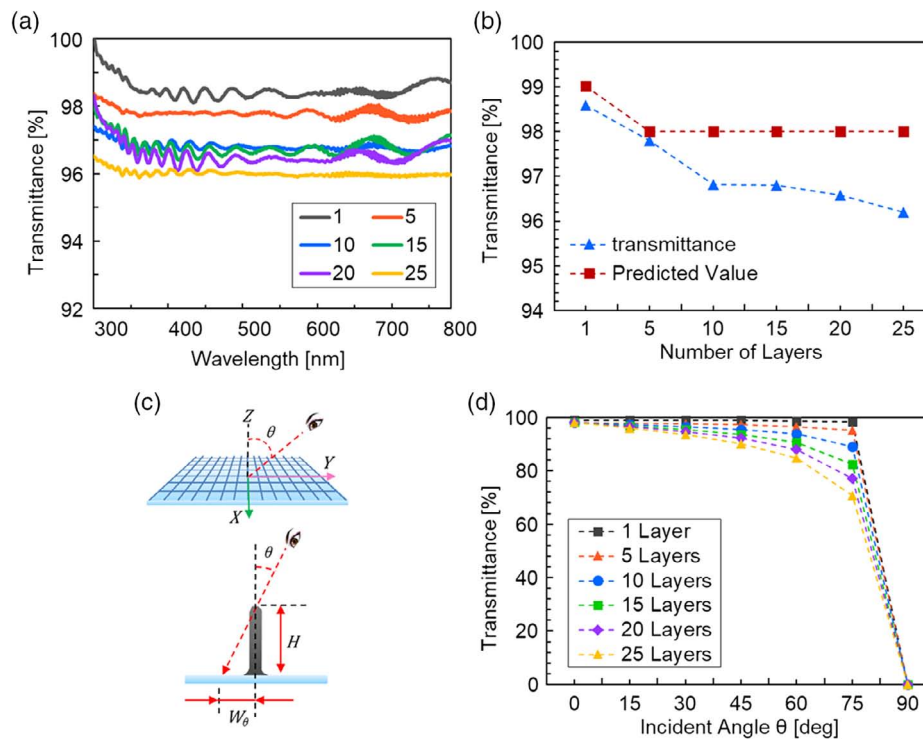
ADVANCED
SCIENCE NEWS
www.advancedsciencenews.com

ADVANCED
ENGINEERING
MATERIALS
www.aem-journal.com

Figure 3. The transmittance of the printed TE. a) The transmittance under different wavelengths from 300 to 800 nm, and the comparison of the number of printed layers, which range from 1 to 25. b) The comparison of predicted value and measured transmittance, which is affected by the number of layers. c) The schematic illustration of the incident angle. d) The effect of the incident angles on transmittance at the different number of layers.

$$T = 1 - F_f \tag{3}$$

The predicted values are also plotted in Figure 3b so as to compare with the experimentally measured data. The total transmittance of the metallic grid was slightly lower than the expected value calculated by the shadowing area. This is due to the large width at the bottom.

In addition, as the thickness of the 3D grid increased, the transmittance decreased due to the large shadowing area. The calculation of the transmittance at different incident angles was carried out to study the effects of metal grids in more detail and evaluate the effects of aspect-ratio. By using the modified equation including the corresponding shadowing area change according to the incident angle, the transmittance could be characterized as

$$F_f = 1 - \frac{(P - \frac{1}{2}W - H\tan\theta)^2}{P^2} \tag{4}$$

where θ represents the incident angle and H is the grid height as shown in Figure 3c. To simplify the condition, the X and Y axis are defined along the grid. The incident angle θ lies in the Z–Y plane. Then, the corresponding shadowing area can be expressed by

$$W_\theta = \frac{1}{2}W + H\tan\theta \tag{5}$$

The influences of Ag grid thickness or number of printed layers on the sheet resistance and transmittance of the 3D metal grid film is shown in Figure 3d. The corresponding shadowing

area gradually increased along with the viewing angle, indicating that the film transmittance decreased. A similar tendency of transmittance decrease could be observed in the different high aspect-ratio 3D grid. This reminds us that the 3D grid height should be controlled in a proper range to guarantee the transmittance. It is necessary to mention that all the numerical estimation equations did not consider the transmittance of the substrate. Therefore, we also set the pure PET film as the reference and the transmittance of the PET film was removed from the measurement results.

Figure 4 shows the measurement of the sheet resistance (R_s) of the TEs. The R_s of the TEs were measured using the four-point probe method, as shown in the inset. Four electrodes, which were deposited on the metallic TEs, separated by an equal distance (20 mm). They were fabricated using the direct dispensing method. To ensure the Ag-NPs connection and electrical conductivity, all the printed TEs were sintered under 200 °C for 1 h. The PEO in the metallic grid could be partly decomposed under this temperature.[42] The Ag 3D grid acted as a large-area high-speed electron-transfer channel. As the thickness of the Ag grid increased, the transmittance and sheet resistance of the hybrid film decreased. Therefore, the sheet resistance decreased from 25 to 3 Ω sq^{-1}, whereas the number of layers increased from 1 to 25. When the printed layer is 25, the average sheet resistance is about 3 Ω sq^{-1} (Figure 4a). From the fill factor, it is also possible to predict sheet resistance by the transparency. For a pattern size that is much larger and wire size that is much smaller than the pitch, the sheet resistance, R_s, is achieved by
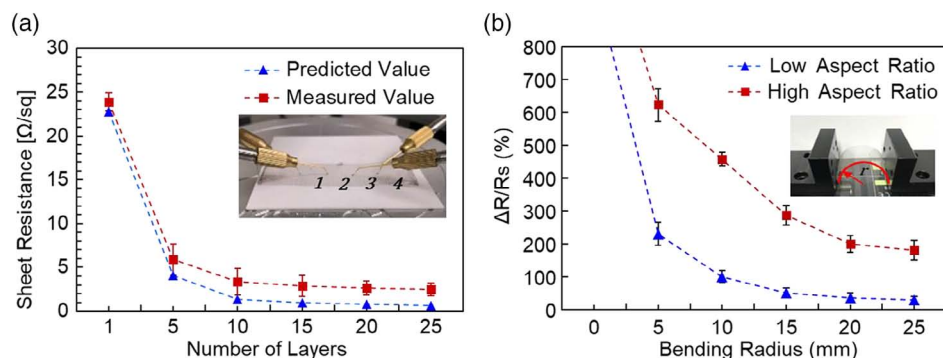
1901275 (5 of 8)

Figure 4. The measurement of sheet resistance (R_s) of the printed TE and bending and recovering test. a) The comparison of predicted R_s with measured R_s, which was conducted by using the four-point probe method. b) TE film bending and recovering test at the different bending radius. The inset photo shows the bending radius. The scale bars in the inset SEM images are both 10 μm.

$$R_s = \xi \frac{\rho_m}{F_f} \times \frac{1}{H} \tag{6}$$

where ρ_m is the electrical resistivity of the printed metallic grid, H is the height of the lines, and ξ is a correction factor depending on the printed material and lattice properties, as well as line and junction imperfections.[29] For a defined fill factor and transparency, an increase in the line height reduces the sheet resistance proportional to $1/H$. The predicted value of R_s is shown in Figure 4a. The experimentally measured value is higher than the predicted one. The average electric conductivity is about 4×10^5 S m^{-1}, which is lower than pure Ag-NPs structures, whose electric conductivity is 5×10^5 S m^{-1}. This is mainly because a small amount of polymer remains in the printed structure and it causes the higher contact resistance between Ag-NPs. The fabricated conducting grids consisted of fairly uniform squares with average widths of 8 μm formed by tightly packed and welded Ag-NPs. We also found that 14 wt% of Ag NPs is the optimal concentration to strike a balance between high conductivity and stable printing conditions. Meanwhile, the contact resistance may cause errors in the electric resistance measurement. Depending on the application, TE based on metallic nanomaterials, such as NWs and grids, should exhibit a sheet resistance in the range of 10–1000 Ω sq^{-1} at a transparency of >90%.[23] Therefore, our printed TEs exhibited high performance both in the electrical conductivity and optical transparency.

The mechanical stability of the 3D metal grid hybrid TE on PET film substrate has been investigated as well. To confirm the influence of substrate bending, two types of Ag grid were prepared on PET substrates and were further bent in different radius. The aspect-ratio of low and high aspect-ratio sample was 10 and 20, respectively. Figure 4b shows the changes in the sheet resistance of the TE film and 3D metallic grid TE film after 50 times bending and recovering at each bending radius. The SEM images which show the detail surface morphology of both low and high aspect-ratio metal grid are plotted in **Figure 5**. The crack appears at the bent grid. The sheet resistance of the tested film remains stable by the bending up to a radius ranging from 20 to 25 mm. When we violently bent the hybrid film at the radius of 15 mm, the crack appeared at the crease place of the 3D metal grid as shown in the inset SEM image.

However, the relative resistance change ($\Delta R / R_s$) of the film only increased over 200% than that of the original value. After 50 times of bending test for 5 mm radius, the sheet resistance increased over 600% compared with the original one. On one hand, both types of TE show that the relative resistance change is inversely proportional to the bending radius. Because the stress on metal grid is inversely proportional to the bending radius, and the crack appeared due to the stress while bending the TE. In contrast, the relative resistance change is more significant for high aspect-ratio TE. When the bending radius is same, the bending stress is proportional to the characteristic length; this means the height of the metal grid. It is believed that such technique is capable of enhancing both mechanical and electrical properties in future transparent flexible electronic devices by improving conductivity and strength of the metallic grid on TEs.

To fully evaluate the performance of a TE, it is necessary to consider both sheet resistance and transmittance. The relationship of the transmittance and sheet resistance for thin transparent conductive films can be expressed by

$$T = \left[1 + \frac{Z_0}{2R_s}\frac{\sigma_{OP}}{\sigma_{DC}}\right]^{-2} \tag{7}$$

where T is the transmittance (wavelength 300–800 nm), Z_0 is the impedance of free space and has the value of 377 Ω,[25,26] R_s is the sheet resistance, σ_{OP} is the optical conductivity, and σ_{DC} is the conductivity of the film. σ_{DC}/σ_{OP} is a commonly used parameter to describe transparent conductors. A large value of σ_{DC}/σ_{OP} indicates good performance of transparent conductors. For the common ITO film with a sheet resistance of $R_s = 10$ Ω sq^{-1} and a transmittance of $T = 90\%$, the σ_{DC}/σ_{OP} ratio is calculated to be 349. In comparison, for our single-layer printed TE that has $R_s = 24$ Ω sq^{-1} and $T = 98.5\%$, the value of $\sigma_{DC}/\sigma_{OP} = 1000$. However, for 25 layers printed TE with $R_s = 2.5$ Ω sq^{-1} and $T = 96.2\%$, the value of σ_{DC}/σ_{OP} reaches over 3900. This exhibits a significantly improved performance than that of ITO. To demonstrate the high performance of 3D metal grid-based TE, we plotted **Figure 6** to show the electrical and optical performances of this work and a comparison between our TE and recently published TEs fabricated by various techniques. Compared with Kim et al. spin-coating fabricated
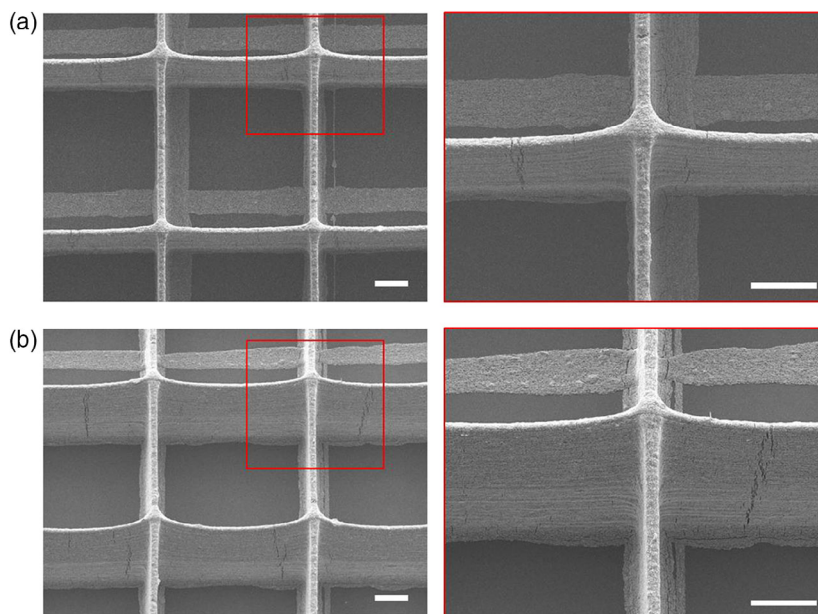
Figure 5. The SEM images of the 3D metal grid detail surface morphology. The low and high aspect-ratio is a) 10 and b) 20, respectively. The magnified SEM images in the red region shows the quality of the grid junction and the crack after bending test.
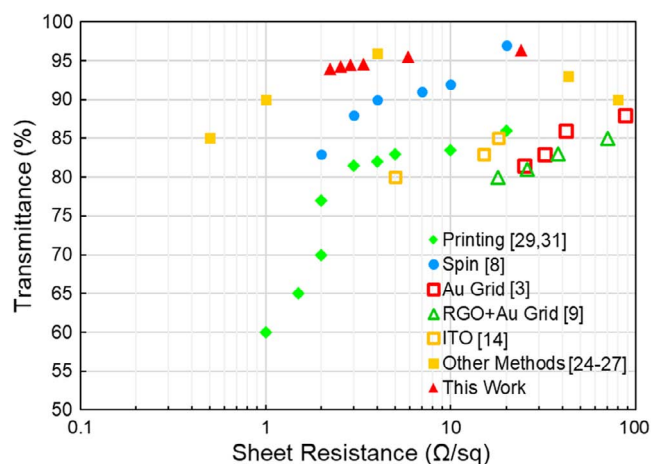

Figure 6. Sheet resistance versus transmittance (without substrate) for this 3D printing work compared with the state-of-the-art methods. The chosen references show the TEs fabricated by printing (29, 31), by spin-coating (8), by laser-sintered Ag grid (3), by reduced graphene oxide and Ag grid (9), traditional ITO films (14) and other methods (24–27).

nanocomposite film as a TE, our results showed a higher transmittance at the same sheet resistance.[8] Our 3D metal grid showed both better optical and electrical performances compared with the previous 2D metal grid, which was fabricated also using the EHD printing technique.[23,25] Other technique that fabricated Ag grid and reduced graphene oxide hybrid TE exhibited similar electric or optical performances compared with ITO glass.[3,9] Therefore, from both numerical and graphic comparisons, it is possible to conclude that 3D metal grid-based TE exhibit both excellent electrical and transmittance performances.

In this article, we present a novel strategy for the fabrication of high-performance TEs via EHD jet-printing technique. The high aspect-ratio 3D metallic grid consisted of Ag-NPs, and the polymer composite was printed directly on the PET film substrates by room-temperature. Micro-scale 3D grids were printed layer-by-layer with an aspect-ratio of above-5. As an application, highly conductive metal grids that exhibit an average sheet resistance of $3\,\Omega\,sq^{-1}$ and transparency of 96% are fabricated and used as high-performance TEs. Also, the flexibility of printed TE was characterized by bending and recovering test. The as-prepared 3D metallic grid-based TE showed excellent optoelectrical properties comparable to those of ITO glass, good flexibility as well as excellent transparent electrode behaviors suitable for the fabrication of next-generation electronic devices with high performances.

Experimental Section

Material and Method: A high-viscosity dispersion of Ag-NPs ink (EM-SP01, Enjet Inc.), which has a viscosity of 10 000 cP and average particle diameters of 100 nm, was used as the main gradient. The Ag-NPs concentration was 70% by weight. The PEO (400 000 MW) ink was diluted by chloroform (Sigma Aldrich, USA) by solid content of 14 wt%. Then, the Ag-NPs paste was mixed with PEO solution by ratio 4:1. The ink was mixed with a stirring magnet for more than 1 h. The ink was kept in a refrigerator at 5 °C to prevent the evaporation of the solvent. The ink was supplied by using a 1 mL Kovax-Syringe plastic syringe (Korea Vaccine Co., Ltd., ROK) that is driven by the remote PHD Ultra cp-4400 syringe pump from Harvard Apparatus Inc. (USA). The selected flow rate was 7.5 µL min⁻¹ during the entirety of the printing process. A 3D printing system (X-model, www.enjet.co.kr) was used in the proposed method. In this system, a high-voltage amplifier is used to generate the DC voltage for the liquid jet. A DC voltage was applied on the nozzle to form a strong electric field that drives the ink droplets toward the substrate. A stainless-steel nozzle, with an inner diameter of 150 µm and outer diameter of 300 µm, was vertically

aligned above a substrate. The distance between the nozzle and target substrate was adjusted by using a Z micro-stage. The XY micro-stage allows for an accurate positioning of the target substrate. The stage movement was controlled by a CAD file for the fabrication of the 3D structures. The substrates were cleaned by using ethanol (Sigma Aldrich, USA). During all the printing works, the humidity and temperature were kept at around 50% and 22 °C, respectively.

Characterizations: All the printing processes were observed using a CCD camera with a light-emitting diode (LED) light source. The printed 3D metallic structures were observed and proved using the field-emission SEM (S-4800, Hitachi). Cross-sectional and 3D profiles of the printed metallic structures were measured by using a 3D profiler (XE-100, Park Systems). The TE transmission of the printed TE was measured by a spectrophotometer (Perkin–Elmer UV–vis-NIR V570, Jasco). The sheet resistance (R_s) of the metallic TEs was approximately measured using the four-point probe method using a microprobe station (MS tech. Model 5500) and a picoammeter (Model 6517 A, Keithley Instruments, Inc., USA). Four electrodes, which were deposited on the metallic TEs and separated by an equal distance (20 mm), were fabricated by using the direct dispensing method.

Fabrication of the 3D Metallic Grid-Based TEs: The transparent conducting electrodes were fabricated on a polyester film. The patterns were controlled within 8 μm width. The fabrication condition was kept at 1.2 kV and a 10 μm working height. After the printing, the sample was cured for 1 h at a temperature of 200 °C to thermal sinter the NPs to increase the conductivity.

Acknowledgements

Conflict of Interest

The authors declare no conflict of interest.

Keywords

[1] M. Song, D. S. You, K. Lim, S. Park, S. Jung, C. S. Kim, D. H. Kim, D. G. Kim, J. K. Kim, J. Park, *Adv. Funct. Mater.* **2013**, *23*, 4177.

[2] M. G. Kang, L. J. Guo, *Adv. Mater.* **2007**, *19*, 1391.

[3] S. Hong, J. Yeo, G. Kim, D. Kim, H. Lee, J. Kwon, H. Lee, P. Lee, S. H. Ko, *ACS Nano* **2013**, *7*, 5024.

[4] K. Zilberberg, F. Gasse, R. Pagui, A. Polywka, A. Behrendt, S. Trost, R. Heiderhoff, P. Görrn, T. Riedl, *Adv. Funct. Mater.* **2014**, *24*, 1671.

[5] D. R. Cairns, R. P. Witte, D. K. Sparacin, S. M. Sachsman, D. C. Paine, G. P. Crawford, R. Newton, *Appl. Phys. Lett.* **2000**, *76*, 1425.

[6] A. R. Rathmell, S. M. Bergin, Y. L. Hua, Z. Y. Li, B. J. Wiley, *Adv. Mater.* **2010**, *22*, 3558.

[7] A. Kumar, C. Zhou, *ACS Nano* **2010**, *4*, 11.

[8] M. Kim, Y. C. Kim, *Synth. Met.* **2014**, *198*, 31.

[9] T. Qiu, B. Luo, M. Liang, J. Ning, B. Wang, X. Li, L. Zhi, *Carbon* **2015**, *81*, 232.

[10] M. Vosgueritchian, D. J. Lipomi, Z. Bao, *Adv. Funct. Mater.* **2012**, *22*, 421.

[11] K. S. Kim, Y. Zhao, H. Jang, S. Y. Lee, J. M. Kim, K. S. Kim, J.-H. Ahn, P. Kim, J.-Y. Choi, B. H. Hong, *Nature* **2009**, *457*, 706.

[12] S. Bae, H. Kim, Y. Lee, X. Xu, J.-S. Park, Y. Zheng, J. Balakrishnan, T. Lei, H. R. Kim, Y. I. Song, *Nat. Nanotechnol.* **2010**, *5*, 574.

[13] D. Y. Choi, H. W. Kang, H. J. Sung, S. S. Kim, *Nanoscale* **2013**, *5*, 977.

[14] Y. Galagan, J.-E. J. Rubingh, R. Andriessen, C.-C. Fan, P. W. Blom, S. C. Veenstra, J. M. Kroon, *Sol. Energy Mater. Sol. Cells* **2011**, *95*, 1339.

[15] M. Layani, R. Berman, S. Magdassi, *ACS Appl. Mater. Interfaces* **2014**, *6*, 18668.

[16] D. S. Hecht, A. M. Heintz, R. Lee, L. Hu, B. Moore, C. Cucksey, S. Risser, *Nanotechnology* **2011**, *22*, 075201.

[17] H. B. Lee, W. Y. Jin, M. M. Ovhal, N. Kumar, J. W. Kang, *J. Mater. Chem. C* **2019**, *7*, 1087.

[18] M. Layani, A. Kamyshny, S. Magdassi, *Nanoscale* **2014**, *6*, 5581.

[19] J. Zou, H.-L. Yip, S. K. Hau, A. K.-Y. Jen, *Appl. Phys. Lett.* **2010**, *96*, 96.

[20] J. Schneider, P. Rohner, D. Thureja, M. Schmid, P. Galliker, D. Poulikakos, *Adv. Funct. Mater.* **2016**, *26*, 833.

[21] W. Y. Jin, R. T. Ginting, K. J. Ko, J. W. Kang, *Sci. Rep.* **2016**, *6*, 36475.

[22] Y. Lee, W. Y. Jin, K. Y. Cho, J. W. Kang, J. Kim, *J. Mater. Chem. C* **2016**, *4*, 757.

[23] A. Khan, S. Lee, T. Jang, Z. Xiong, C. Zhang, J. Tang, W. D. Li, *Small* **2016**, *12*, 3021.

[24] F. M. Wisser, K. Eckhardt, W. Nickel, W. Böhlmann, S. Kaskel, J. Grothe, *Mater. Res. Bull.* **2018**, *98*, 231.

[25] Y. S. Oh, H. Lee, D. Y. Choi, S.-U. Lee, H. Kim, S. Yoo, I. Park, H. J. Sung, *ACS Appl. Mater. Interfaces* **2016**, *8*, 10937.

[26] Y. S. Oh, H. Choi, J. Lee, H. Lee, D. Y. Choi, S.-U. Lee, K.-S. Yun, S. Yoo, T.-S. Kim, I. Park, *Sci. Rep.* **2017**, *7*, 11220.

[27] Y. Lee, W.-Y. Jin, K. Y. Cho, J.-W. Kang, J. Kim, *J. Mater. Chem. C* **2016**, *4*, 7577.

[28] A. D. Printz, E. Chan, C. Liong, R. S. Martinez, D. J. Lipomi, *PloS One* **2013**, *8*, e83939.

[29] B. Seong, H. Yoo, V. D. Nguyen, Y. Jang, C. Ryu, D. Byun, *J. Micromech. Microeng.* **2014**, *24*, 097002.

[30] H.-J. Choi, S. Choo, P.-H. Jung, J.-H. Shin, Y.-D. Kim, H. Lee, *Nanotechnology* **2015**, *26*, 055305.

[31] K. Kim, D. S. Park, H. M. Lu, W. Che, K. Kim, J.-B. Lee, C. H. Ahn, *J. Micromech. Microeng.* **2004**, *14*, 597.

[32] A. Del Campo, C. Greiner, *J. Micromechan. Microeng.* **2007**, *17*, R81.

[33] M. S. Onses, E. Sutanto, P. M. Ferreira, A. G. Alleyne, J. A. Rogers, *Small* **2015**, *11*, 4237.

[34] K. Sun, T. S. Wei, B. Y. Ahn, J. Y. Seo, S. J. Dillon, J. A. Lewis, *Adv. Mater.* **2013**, *25*, 4539.

[35] S. H. Ko, J. Chung, N. Hotz, K. H. Nam, C. P. Grigoropoulos, *J. Micromechan. Microeng.* **2010**, *20*, 125010.

[36] B. W. An, K. Kim, H. Lee, S. Y. Kim, Y. Shim, D. Y. Lee, J. Y. Song, J. U. Park, *Adv. Mater.* **2015**, *27*, 4322.

[37] S. Z. Guo, F. Gosselin, N. Guerin, A. M. Lanouette, M. C. Heuzey, D. Therriault, *Small* **2013**, *9*, 4118.

[38] B. Zhang, B. Seong, J. Lee, V. Nguyen, D. Cho, D. Byun, *ACS Appl. Mater. Interfaces* **2017**, *9*, 29965.

[39] H.-Y. Kim, M. Lee, K. J. Park, S. Kim, L. Mahadevan, *Nano Lett.* **2010**, *10*, 2138.

[40] N. Kojic, M. Kojic, S. Gudlavalleti, G. McKinley, *Biomacromolecules* **2004**, *5*, 1698.

[41] B. Seong, I. Chae, H. Lee, V. D. Nguyen, D. Byun, *Phys. Chem. Chem. Phys.* **2015**, *17*, 7629.

[42] A. Nijenhuis, E. Colstee, D. Grijpma, A. Pennings, *Polymer* **1996**, *37*, 5849.